Base-Profile Optimization for Minimum Noise Figure in Advanced UHV/CVD SiGe HBT's

William E. Ansley, *Student Member, IEEE,* John D. Cressler, *Senior Member, IEEE,* and David M. Richey, *Member, IEEE*

***Abstract*— We investigate the base-profile design issues associated with optimizing ultrahigh vacuum/chemical vapor deposition (UHV/CVD) silicon–germanium (SiGe) heterojuction bipolar transistors (HBT's) for minimum broad-band noise. Using the simulator for cryogenic research and SiGe bipolar device optimization (SCORPIO), the impact of Ge profile, base doping level, and base thickness on minimum noise figure ($\mathrm{NF}_{\min}$) are quantitatively examined across the -55 °C–125 °C temperature range. We introduce a novel Ge profile for optimum $\mathrm{NF}_{\min}$, which allows independent control of current gain (β) and achieves maximum f_T while maintaining thermodynamic stability. Simulations show that this profile can achieve a β of ~200, a peak $f_T > 50$ GHz, a peak $f_{\max} > 60$ GHz, and an $\mathrm{NF}_{\min} < 0.5$ dB at 2 GHz and <1 dB at 10 GHz using a conservative base width of ~90 nm. We predict that a 45-nm base-width/0.5-μm emitter-width device with a thermodynamically stable flat Ge profile, manufacturable using an UHV/CVD growth technique, should be able to achieve an $\mathrm{NF}_{\min} < 0.4$ dB at 2 GHz and ~0.8 dB at 10 GHz along with a β of ~300, a peak $f_T > 70$ GHz, and a peak $f_{\max} > 90$ GHz. These 300-K performance values improve as the temperature is reduced.**

***Index Terms*—Heterojunction bipolar transistors, germanium, semiconductor device modeling, semiconductor device noise, silicon.**

I. Introduction

SILICON–GERMANIUM (SiGe) heterojunction bipolar transistors (HBT's) offer many performance advantages over Si bipolar junction transistors (BJT's), including higher common-emitter dc-current gain (β), transition frequency (f_T), and maximum oscillation frequency ($f_{\max}$), and have excellent broad-band noise characteristics [1], [2]. Our investigation uses the one-dimensional (1-D) drift–diffusion simulator for cryogenic research and SiGe bipolar device optimization (SCORPIO) to generate current densities, β, transit times, f_T, intrinsic base sheet resistance (R_{bi}), capacitances, and other bias-dependent parameters from secondary ion mass spectroscopy (SIMS) doping and Ge profiles. These results are then combined with assumptions on the lateral geometry of the device and extrinsic parasitics in order to calculate $f_{\max}$ and minimum noise figure ($\mathrm{NF}_{\min}$). The simulation results presented assume an advanced bipolar technology which allows a 0.5-μm emitter width, silicided double-base contacts, and 0.25-μm oxide sidewall spacer thickness. The noise model used is that presented by Hawkins [3]. This simulation approach gives good agreement with measured data (see Fig. 1) [2].

Manuscript received September 8, 1997; revised January 9, 1998. This work was supported by DARPA under Contract N66001-96-C-8624.

W. E. Ansley and J. D. Cressler are with the Electrical Engineering Department, Auburn University, Auburn, AL 36849 USA.

D. M. Richey is with Lucent Technologies, Allentown, PA 18103 USA.

Publisher Item Identifier S 0018-9480(98)03390-0.

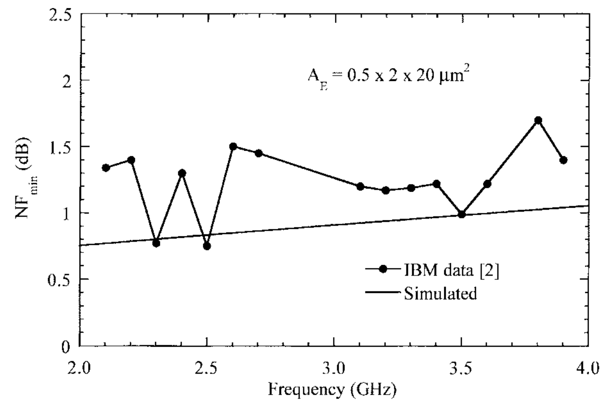

Fig. 1. Comparison of simulated $\mathrm{NF}_{\min}$ with measured data from an IBM SiGe HBT with emitter dimensions (A_E) of 0.5 × 2 × 20 μm^2 [2].

II. The SCORPIO Simulator

SCORPIO is a 1-D drift–diffusion device simulation program specifically developed for investigating the SiGe HBT over a wide range of temperatures [4], [5]. SCORPIO has full heterojunction simulation capability, advanced parameter models for mobility, transit time, and bandgap narrowing, and provides both bias- and position-dependent output. It has been shown to have excellent agreement with measured data for advanced SiGe HBT's grown using the ultrahigh vacuum/chemical vapor deposition (UHV/CVD) technique from 300 K down to liquid-nitrogen temperature (77 K) [6]–[8].

SCORPIO uses a doping and Ge profile, such as the one shown in Fig. 2, as the input data file. This profile represents an actual state-of-the-art SiGe HBT designed for high-performance analog-circuit applications [9] and will be referred to as the "calibrated profile." It is a trapezoidal profile which varies linearly from 1% to 10.5% Ge and has a relatively conservative metallurgical base width of approximately 90 nm. Such profile input files can either be generated from measured SIMS data or from process simulators such as TSUPREM-4. Fig. 3 shows the five Ge profiles used to investigate the impact of the Ge profile on minimum noise figure. All of these profiles have an approximately 25-nm-thick Si cap layer, the same effective thickness (depth from the crystalline surface of the wafer to the Ge at the collector–base (CB) junction), and the same effective average Ge content (average amount of Ge in

0018–9480/98$10.00 © 1998 IEEE

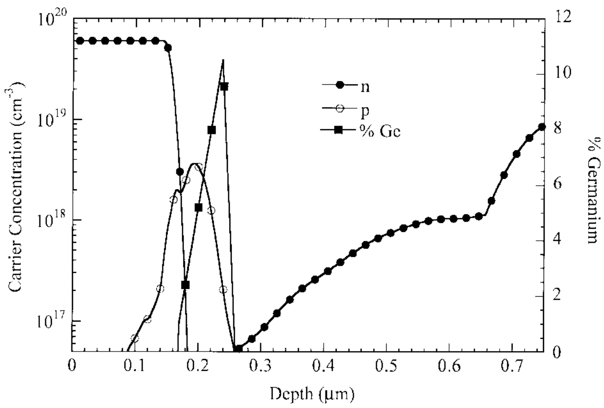

Fig. 2. Doping profile (from SIMS data) for an SiGe HBT with a 1%–10.5% trapezoidal Ge profile which has been used to calibrate SCORPIO to measured data (“calibrated profile”).

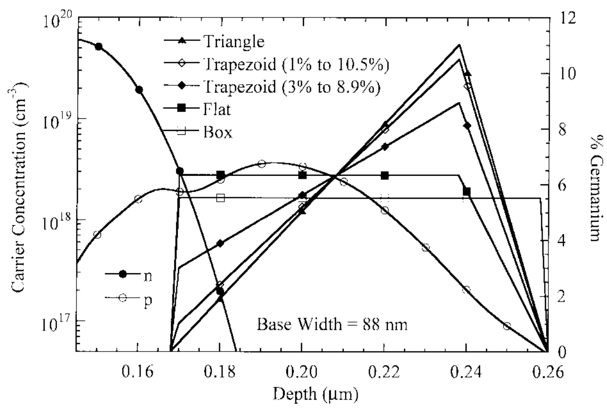

Fig. 3. Five commonly used Ge profiles having the same thermodynamic stability. Included is the calibrated profile (1%–10.5% trapezoid). The emitter and base carrier concentrations are shown from the poly-Si-to-Si interface in the emitter (at left edge) to the base–collector metallurgical junction (at right edge).

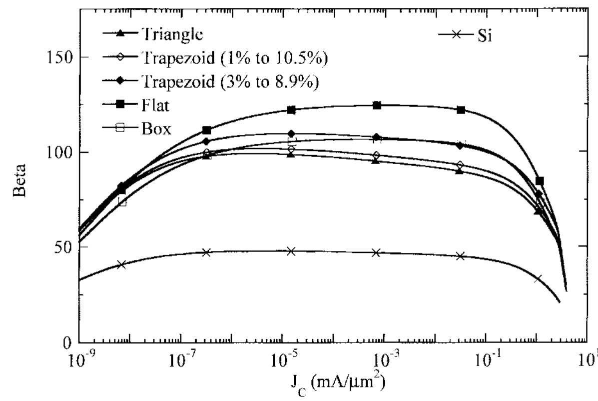

Fig. 4. Simulated β for the five Ge profiles shown in Fig. 3 along with an Si BJT control. The presence of Ge greatly enhances β and the bias dependence is dependent on profile.

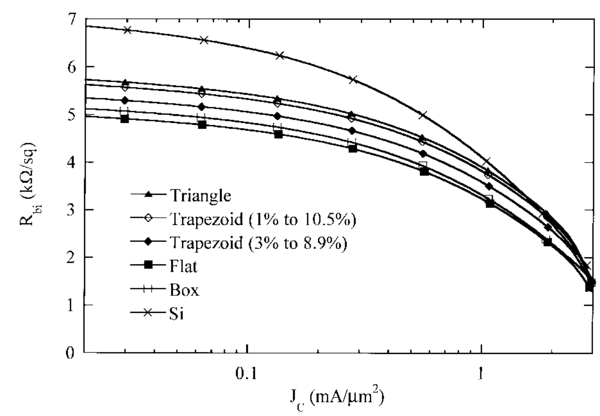

Fig. 5. Simulated R_{bi} for the five Ge profiles shown in Fig. 3 along with an Si BJT control. The presence of Ge reduces R_{bi}.

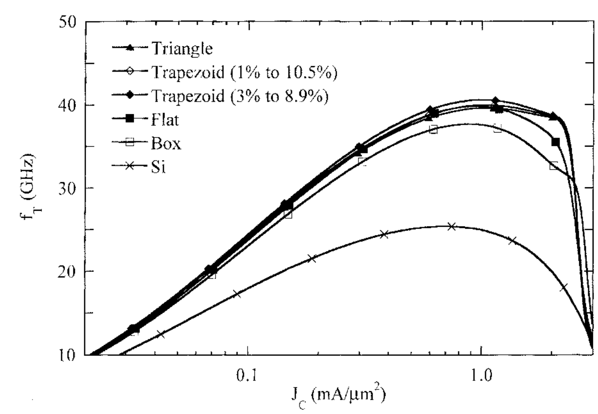

Fig. 6. Simulated f_T for the five Ge profiles shown in Fig. 3 along with an Si BJT control. The presence of Ge increases f_T, but is not strongly dependent on profile.

the effective thickness) and, thus, equivalent thermodynamic stability [10]–[13].

For the work presented here, the CB bias $(V_{\rm CB})$ is fixed at 1 V and the base–emitter bias $(V_{\rm BE})$ is stepped up from 0 to 1 V. Figs. 4–6 show β, R_{bi}, and f_T, respectively, for the five profiles along with the Si BJT control. Notice in Fig. 4, that the presence of Ge greatly enhances β. Both theory and experimental results show that this is primarily controlled by the exponential dependence of β on the Ge-induced bandgap narrowing at the base-side edge of the emitter–base (EB) depletion region $[\Delta E_{g,Ge}(x_o)]$ [6], [14]. Notice also, that the graded Ge profiles show a slight decrease in β with increasing collector current density. This is because the EB depletion region shrinks as $V_{\rm BE}$ is increased, effectively reducing $\Delta E_{g,Ge}(x_o)$ with increasing bias (i.e., the “Ge-ramp” effect) [14].

R_{bi} is the sheet resistance of the neutral base region and, for an n-p-n transistor under low-level injection bias conditions (as is the case for low-noise operation), is given by

$$R_{bi} = \frac{1}{\displaystyle\int_{x_o}^{x_w} q\mu_p(x) N_A^-(x)\, dx} \qquad (1)$$

where x_o is the base-side edge of the EB depletion region, x_w is the base-side edge of the CB depletion region, $\mu_p(x)$ is the majority-carrier hole mobility as a function of position, and $N_A^-(x)$ is the ionized acceptor doping concentration in the base as a function of position (which is approximately equal to the p-doping level). The exact functional form of the dependence of majority-carrier hole mobility enhancement in strained

SiGe film layers, as compared to Si, is an unresolved and actively investigated area among many groups. Additionally, the diffusion of boron in strained SiGe is known to be slower than in Si, thus making it difficult to make a true one-to-one mobility comparison. At least for the doping ranges used in this paper, the presence of Ge reduces R_{bi}. Our simulations assume that the base doping profile is constant and use a mobility model which gives excellent agreement with measured R_{bi} data over a wide temperature range [6]. The impact of the Ge profile can be seen in Fig. 5. Referring to Fig. 3, observe that the peak in base doping occurs at a depth between 0.190 and 0.195 μm. For the different profiles, the higher the Ge content in this range, the lower the R_{bi} obtained.

As shown in Fig. 6, the presence of Ge increases f_T, although there is not a strong dependence on the profile. f_T is given by

$$f_T = \frac{1}{2\pi(\tau_b + \tau_e + \tau_c + \tau_{\rm eb} + \tau_{\rm cb})} \tag{2}$$

where τ_b, τ_e, and τ_c are the base, emitter, and collector transit times, respectively, and $\tau_{\rm eb}$ and $\tau_{\rm cb}$ represent the EB and CB depletion layer capacitance charging times, respectively. The two transit times which dominate f_T in modern Si bipolar transistors are the τ_b and τ_e. For an SiGe HBT, a grading of Ge across the neutral base induces a drift field in the base, which accelerates the electrons injected from the emitter to the collector, thereby decreasing τ_b. The ratio of τ_b for ideal SiGe and Si devices of identical doping profiles is given by [15]

$$\frac{\tau_{b,\rm SiGe}}{\tau_{b,\rm Si}} = \frac{2kT}{\lambda \cdot \Delta E_{g,\rm Ge}(\text{grade})} \cdot \left[1 - \frac{(1 - \exp[-\Delta E_{g,\rm Ge}(\text{grade})/kT])}{\Delta E_{g,\rm Ge}(\text{grade})/kT}\right] \tag{3}$$

where λ accounts for the strain induced-mobility enhancement and

$$\Delta E_{g,\rm Ge}(\text{grade}) = \Delta E_{g,\rm Ge}(x_w) - \Delta E_{g,\rm Ge}(x_o). \tag{4}$$

$\Delta E_{g,\rm Ge}(x_w)$ represent the Ge-induced bandgap narrowing at the base-side edges of the CB depletion region. The ratio of τ_e for ideal SiGe and Si devices of identical doping profiles is given by [15]

$$\frac{\tau_{e,\rm SiGe}}{\tau_{e,\rm Si}} \simeq \frac{\beta_{\rm Si}}{\beta_{\rm SiGe}}. \tag{5}$$

As the Ge at x_o enhances β, it produces a strong reduction in τ_e. Therefore, there exists a tradeoff between τ_b and τ_e for different Ge profiles having the same thermodynamic stability, which accounts for the weak f_T dependence on profile. The simulated peak f_T of the calibrated profile agrees to within 10% of the experimentally measured value of 43 GHz.

III. Extrinsic Parasitics

For well-behaved modern Si technologies, the 1-D approximations required to use SCORPIO should be extremely accurate for the parameters which it calculates. And in fact, SCORPIO results have been shown to have excellent agreement with measured data (over a wide temperature range)

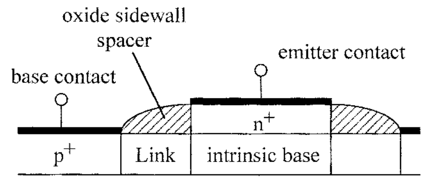

Fig. 7. Schematic cross section showing the location of the oxide sidewall spacer and base link-resistance implant with respect to the base and emitter contacts (not to scale).

[6]–[8]. However, there are other common figures of merit which are of interest to device designers. In order to extend the 1-D output data from SCORPIO, assumptions must be made on the lateral geometry of the device and the extrinsic parasitics. We assume a 0.5-μm emitter-width structure with silicided double-base contacts and 0.25-μm oxide sidewall spacer thickness. We further assume 1-μm metal linewidths and spacings, and that the device has deep-trench isolation at the outside edges of the base metal. This is necessary to estimate the extrinsic CB capacitance ($C_{\rm cbx} = 0.21$ fF/μm^2) and extrinsic base resistance (R_{bx}). It is also assumed that there is a base link resistance implant under the oxide sidewall spacer which dominates R_{bx}. Fig. 7 illustrates where this link resistance is located.

Once values for these extrinsic parasitics have been estimated, $f_{\max}$ can be calculated by

$$f_{\max} = \sqrt{\frac{f_T}{8\pi R_b C_{\rm cb}}} \tag{6}$$

where the total base resistance (R_b) is given by

$$R_b = R'_{bi} + \frac{R_{bx}}{2} \tag{7}$$

the intrinsic base resistance (R'_{bi}) for devices with double base contacts is given by

$$R'_{bi} = \frac{1}{12}\left(\frac{\text{emitter width}}{\text{emitter length}}\right) R_{bi} \tag{8}$$

and the total CB junction capacitance ($C_{\rm cb}$) is given by

$$C_{\rm cb} = C_{\rm cbi} + C_{\rm cbx}. \tag{9}$$

R_{bi} and the intrinsic CB capacitance ($C_{\rm cbi}$) are calculated by SCORPIO. The emitter length multiplies out of the $f_{\max}$ calculation if the end effects of the transistor are neglected. This should be a valid assumption for emitter lengths greater than about 10 μm.

Fig. 8 shows $f_{\max}$ of the calibrated profile for a range of base link sheet-resistances. 6000 $\Omega/\square$ corresponds roughly to no additional doping in the link region and 200 $\Omega/\square$ represents an aggressive additional doping step. As can be seen, $f_{\max}$ is highly sensitive to how this link region is designed, and the link resistance should be minimized. Decreasing the oxide sidewall spacer thickness will also serve to reduce the link resistance.

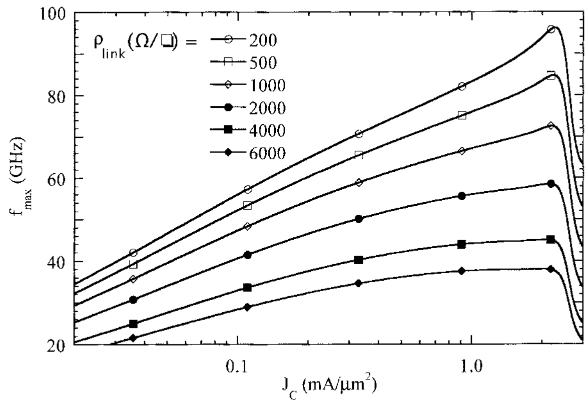

Fig. 8. $f_{\max}$ for the calibrated profile for a range of base link sheet-resistance values. $f_{\max}$ is highly sensitive to how the base link region is designed.

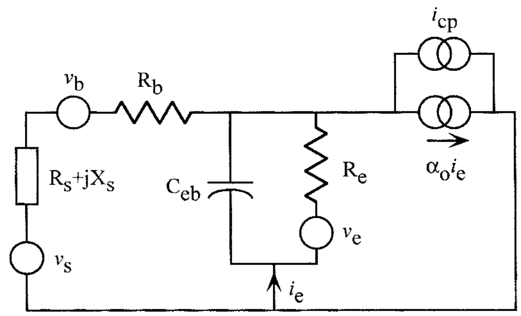

Fig. 9. Equivalent circuit schematic of Hawkins' noise model for bipolar transistors [3].

IV. Noise Model

The noise model used in this paper is that presented by Hawkins [3], the equivalent-circuit schematic of which is shown in Fig. 9. This model accounts for the thermal noise in the source (v_s) and base (v_b) resistances, the shot noise in the emitter (v_e), and the collector partition noise $(i_{\rm cp})$. The resulting expression for noise factor can be written as (10), shown at the bottom of the page, where R_s is the source resistance, X_s is the source reactance, R_e is the dynamic emitter resistance (thermal voltage divided by emitter current), $C_{\rm eb}$ is the EB depletion capacitance $(C_{\rm eb} = \tau_{eb}/R_e)$, α_o is the common-base dc-current gain, $|\alpha|$ is the magnitude of the common-base small-signal ac-current gain, and f is the frequency at which the noise factor is evaluated. This formulation allows one to isolate the base thermal (second term), emitter shot (third term), and collector partition (fourth term) noise sources (all normalized by the source thermal noise). Even though the complete expression is used in our calculations, a simplified version accounting only for the dominant terms can be expressed as

$$F \cong 1 + \frac{R_b}{R_s} + \frac{R_e}{2}\left[\frac{(1-(2\pi f)C_{\rm eb}X_s)^2}{R_s} + ((2\pi f)C_{\rm eb})^2 R_s\right] + \left(\frac{1+(2\pi f)^2\tau_b^2}{\alpha_o} - 1\right)\left(\frac{R_s}{2R_e} + \frac{X_s^2}{2R_eR_s}\right). \quad (11)$$

This formulation helps in determining which parameters are controlling the noise factor. Generally speaking, the presence of Ge reduces the noise factor by decreasing τ_b, decreasing R_b (through R_{bi}), and allowing nearly independent control of β. $\mathrm{NF}_{\min}$ is given by $10 \cdot \log(F)$ when R_s is set to the optimum source resistance $(R_{\rm opt})$. $R_{\rm opt}$ is given by

$$R_{\rm opt} = \sqrt{R_b^2 - X_{\rm opt}^2 + \frac{1+(2\pi f)^2\tau_b^2}{\alpha_o}\frac{R_e(2R_b+R_e)}{a}} \quad (12)$$

where the optimum source reactance $(X_{\rm opt})$ is given by

$$X_{\rm opt} = \frac{1+(2\pi f)^2\tau_b^2}{\alpha_o}\frac{(2\pi f)C_{\rm eb}R_e^2}{a} \quad (13)$$

and

$$a = [(1+((2\pi f)\tau_b)^2)(1+((2\pi f)\tau_{\rm eb})^2) - \alpha_o]\frac{1}{\alpha_o}. \quad (14)$$

Accounting only for the dominant terms, these equations simplify to

$$R_{\rm opt} \cong \sqrt{\frac{2R_bR_e}{a} + \left(\frac{R_e^2}{2} - X_{\rm opt}^2\right)} \quad (15)$$

$$X_{\rm opt} \cong \frac{(2\pi f)C_{\rm eb}R_e^2}{a} \quad (16)$$

and

$$a \cong \frac{1}{\beta} + \frac{((2\pi f)\tau_b)^2}{\alpha_o} + \frac{((2\pi f)\tau_{\rm eb})^2}{\alpha_o}. \quad (17)$$

Note that the length of the emitter has no impact on the noise figure because each term consists of a resistance normalized by the source resistance (once again, neglecting end effects). However, the optimum source resistance is linearly impacted by the emitter length and can be used in sizing the device from a high-frequency matching standpoint.

Fig. 10 shows $\mathrm{NF}_{\min}$ at 10 GHz for the calibrated profile over the range of base link sheet resistances used in the $f_{\max}$ calculations. Like $f_{\max}$, $\mathrm{NF}_{\min}$ is highly sensitive to how this region is designed and the link resistance should be minimized. An aggressive base link sheet resistance of 500 Ω/□ is assumed in the remainder of this paper. Fig. 11 shows the contributions of each of the three noise sources in terms of noise factor. Realizing from Fig. 10 that the minimum $\mathrm{NF}_{\min}$ occurs at a current density of about 0.1 mA/μm^2, it can

$$F = 1 + \frac{R_b}{R_s} + \frac{R_e}{2R_s}[(1-(2\pi f)C_{\rm eb}X_s)^2 + (2\pi f)^2C_{\rm eb}^2(R_s+R_b)^2] + \left(\frac{\alpha_o}{|\alpha|^2} - 1\right)\frac{[R_s + R_b + R_e(1-(2\pi f)C_{\rm eb}X_s)]^2 + [X_s + (2\pi f)C_{\rm eb}R_e(R_s+R_b)]^2}{2R_eR_s} \quad (10)$$

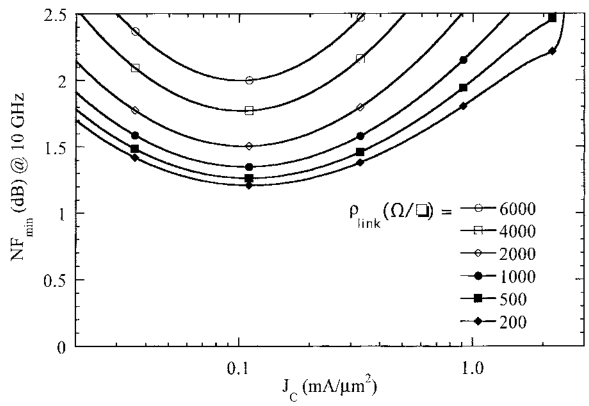

Fig. 10. $\mathrm{NF}_{\min}$ for the calibrated profile for a range of base link sheet-resistance values.

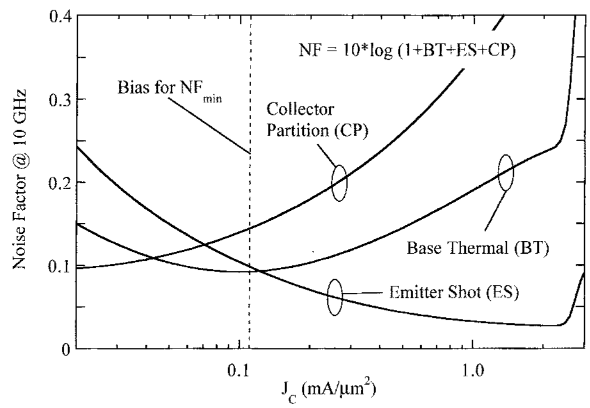

Fig. 11. Relative contributions of the noise-factor sources for the calibrated profile using a base link sheet resistance of 500 $\Omega/\Box$.

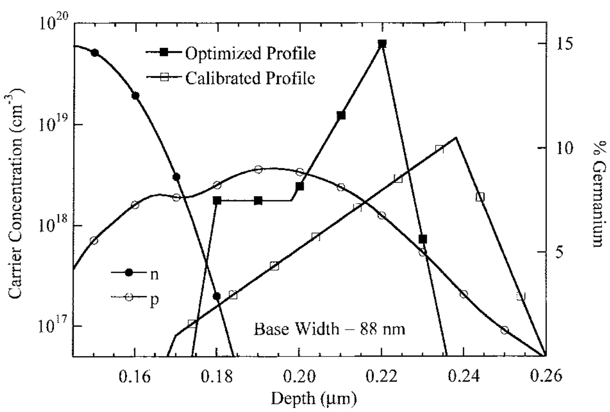

Fig. 12. Novel Ge profile which allows optimization for $\mathrm{NF}_{\min}$ along with the "calibrated profile" (1%–10.5% trapezoid). The emitter and base carrier concentrations are shown from the poly-Si-to-Si interface in the emitter (at left edge) to the base–collector metallurgical junction (at right edge).

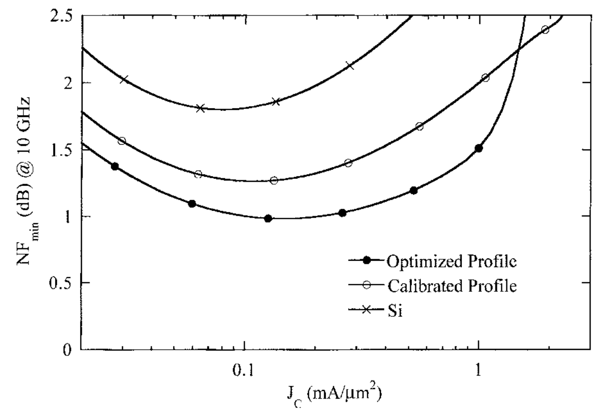

Fig. 13. $\mathrm{NF}_{\min}$ comparison at 10 GHz for the Si BJT, calibrated profile, and optimized profile using a base link sheet resistance of 500 $\Omega/\Box$.

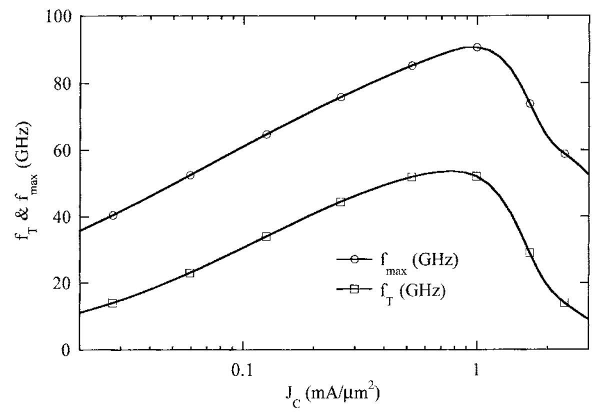

Fig. 14. f_T and $f_{\max}$ for the optimized profile using a base link sheet resistance of 500 $\Omega/\Box$.

be seen in Fig. 11 that the collector partition noise dominates. Thus, from the forth term in (11), we see that increasing β (and thus, α_o) will serve to reduce $\mathrm{NF}_{\min}$ below the 1.3 dB predicted here. And, in fact, the flat Ge profile (which has the highest β) offers a slightly lower $\mathrm{NF}_{\min}$ of 1.25 dB.

Strictly considering the Ge profile, the best noise performance will be achieved with the greatest amount of Ge in the neutral base region. The limitations on the amount of Ge are the thermodynamic stability limit and the maximum acceptable β. In Fig. 12, we introduce a new thermodynamically stable Ge profile which makes optimum use of the Ge to achieve a minimum $\mathrm{NF}_{\min}$. This "optimized profile" provides constant Ge at the EB junction for improved β bias dependence and maximum β in the bias range of interest. It is the level of Ge in this flat region which determines β. The Ge at the CB junction is slid toward the emitter to achieve higher peak Ge percentages at a similar stability. This can be done since minimum $\mathrm{NF}_{\min}$ occurs at a much lower current density than does peak $f_{\max}$ (see Fig. 8) and, thus, before the onset of Ge-induced high injection-barrier effects [7]. The remaining Ge (from the stability standpoint) is put into the Ge grading to decrease τ_b. The resulting Ge profile produces a β of ~200, a peak $f_T > 50$ GHz, a peak $f_{\max} > 60$ GHz, and a $\mathrm{NF}_{\min} < 0.5$ dB at 2 GHz and <1 dB at 10 GHz at a conservative base width of 90 nm. This is compared to <0.9 dB at 2 GHz and <1.8 dB at 10 GHz for the Si BJT control. Fig. 13 compares $\mathrm{NF}_{\min}$ at 10 GHz for the Si BJT, the calibrated profile, and the optimized profile. Fig. 14 shows the frequency response of the optimized profile. The peaks in both f_T and $f_{\max}$ occur at lower current densities than the calibrated profile as a direct result of having slid the Ge at the CB junction toward the emitter. Doing this causes the onset of Ge-induced high injection-barrier effect to occur at a

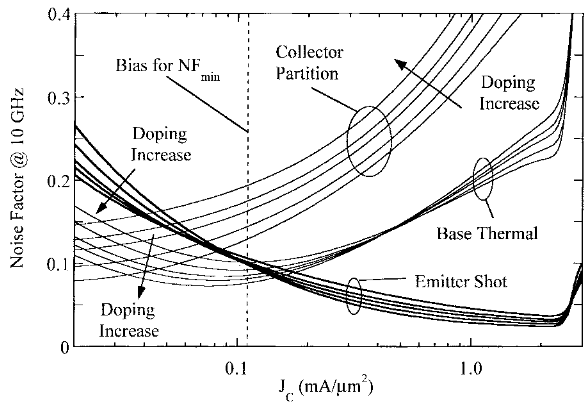

Fig. 15. Effect of base doping level on the noise factor sources for the calibrated profile using a base link sheet resistance of 500 $\Omega/\Box$.

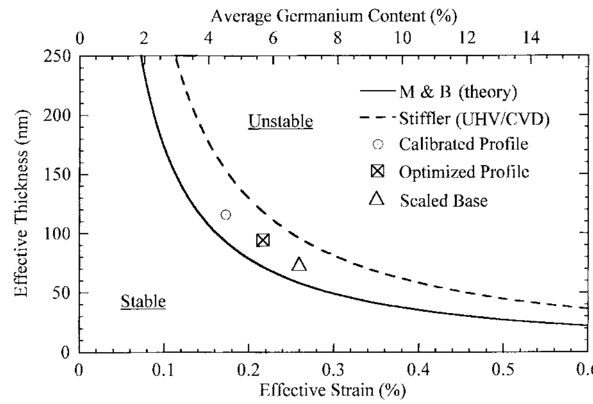

Fig. 16. Stability space plot showing location of the Ge profiles presented.

lower current density. This effect can also be seen in the sharp increase in $\mathrm{NF_{min}}$ above 1 mA/μm^2. For low-noise devices, this is an acceptable tradeoff because the device will most likely be biased at or near the bias corresponding to minimum $\mathrm{NF_{min}}$.

V. Impact of Base Doping

Base doping has a direct impact on β, R_{bi}, and f_T, with all decreasing as the doping level increases. The decrease in β and f_T (with increases in both τ_b and τ_e) would lead one to expect $\mathrm{NF_{min}}$ to increase. However, the decrease in R_{bi} suggests that maybe there will be a decrease in $\mathrm{NF_{min}}$. The optimum base doping level depends on which noise terms dominate $\mathrm{NF_{min}}$. The base doping is varied by scaling the peak of the calibrated profile by 0.75×, 1×, 1.25×, 1.5×, and 2×. The emitter and collector profiles remain unchanged so as to maintain constant C_{cb} and an open-base breakdown voltage (BV_{CEO}) of 3.3 V (experimentally determined for the calibrated profile). For the 90-nm base-width devices in the doping range investigated, the collector partition noise dominates. Thus, as can be seen in Fig. 15 for the calibrated profile, increasing base doping increases $\mathrm{NF_{min}}$ because β decreases and τ_b increases. Even though an increase in doping reduces R_b, R_{opt} also decreases to partially offset the impact on the base thermal-noise component.

Typically, there are a number of other issues and device specifications which influence the optimum base doping level. If the base doping level is too low, current crowding could become a problem. This occurs when R_{bi} gets high enough to cause a bias variation across the EB junction. Decreasing the base doping level may also cause β to become unacceptably high. Also, as is the case for the devices investigated here, the increase in R_{bi} can offset the increase in f_T and cause a decrease in $f_{\max}$ with decreased doping.

VI. Impact of Base Thickness

A scaled base thickness is achieved by decreasing the distance between the EB and CB metallurgical junctions by a factor of two, thus reducing the total doping in the metallurgical base by one-half. The emitter and collector profiles remain unchanged. Fig. 16 shows the locations of all

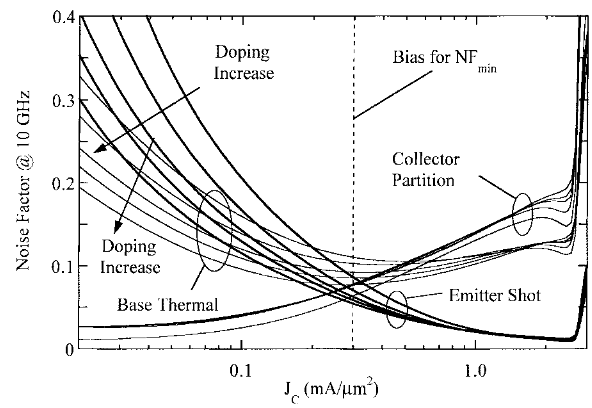

Fig. 17. Effect of base doping level on the noise factor sources for the scaled base profile using a base link sheet resistance of 500 $\Omega/\Box$.

of the Ge profiles in stability space. Interestingly, comparisons indicate that thinning the base alone does not necessarily increase $f_{\max}$ or reduce $\mathrm{NF_{min}}$. From the noise standpoint, one of the primary advantages to thinning the base is that higher Ge content can be used while remaining thermodynamically stable. This is illustrated by the "Scaled Base" point in Fig. 16. Simulations show that collector partition noise no longer dominates at this base thickness (see Fig. 17), nor does it increase with increasing doping since R_{opt} decreases faster with increasing doping in the thinner devices. Therefore, increasing doping goes to reducing the base thermal noise (by reducing R_b) and the emitter shot noise (through R_{opt}). Using a 2× increase in the doping level, we predict a β of $\sim$300, a peak $f_T > 70$ GHz, a peak $f_{\max} > 90$ GHz, and a $\mathrm{NF_{min}} < 0.4$ dB at 2 GHz and $\sim$0.8 dB at 10 GHz using a thermodynamically stable, flat 11.9% Ge profile in a manufacturable SiGe HBT technology.

VII. Temperature Effects

It is a common practice to operate low-noise devices at low temperature in an effort to reduce $\mathrm{NF_{min}}$. However, this does not necessarily reduce the noise generated in bipolar transistors. Fig. 18 shows the minimum values of $\mathrm{NF_{min}}$ for the calibrated profile, optimized profile, scaled base device with a flat Ge profile and 2× increase in base doping, and Si control over the temperature range from −55 °C to 125 °C.

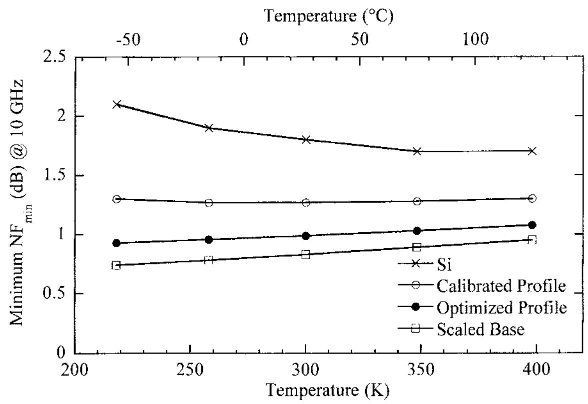

Fig. 18. Minimum $\mathrm{NF}_{\min}$ at 10 GHz for the Si, calibrated profile, optimized profile, and scaled base profile as a function of temperature using a base link sheet resistance of 500 $\Omega/\square$.

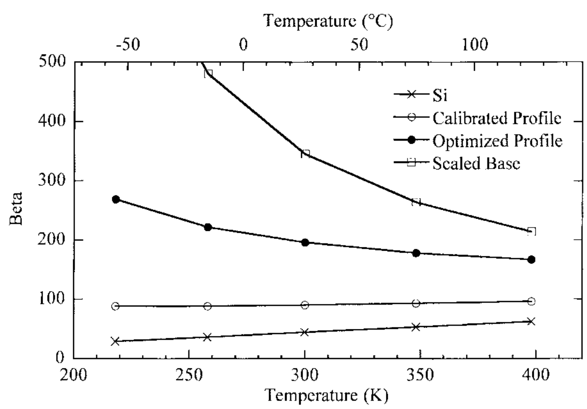

Fig. 19. β for the Si, calibrated profile, optimized profile, and scaled base profile as a function of temperature.

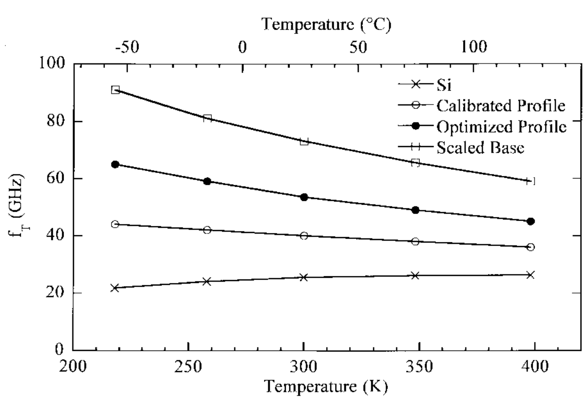

Fig. 20. f_T for the Si, calibrated profile, optimized profile, and scaled base profile as a function of temperature.

Simulations show that $\mathrm{NF}_{\min}$ increases in the Si control and remains roughly unchanged in the calibrated profile as the temperature is reduced, whereas the optimized and scaled base profiles show a decrease in $\mathrm{NF}_{\min}$ as the temperature is reduced. The reasons for these trends are illustrated in Figs. 19 and 20. In Fig. 19, we see that reducing the temperature drives β sharply upward in the optimized and scaled base profiles, leading to a sharp decrease in the collector partition noise component. This is not the case with the calibrated profile, and

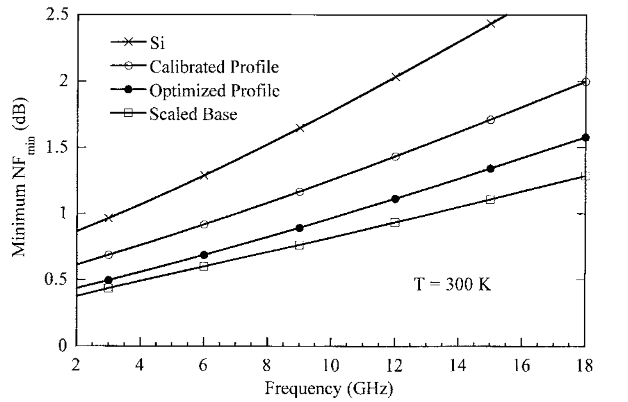

Fig. 21. $\mathrm{NF}_{\min}$ for the Si, calibrated profile, optimized profile, and scaled base profile as a function of frequency using a base link sheet resistance of 500 $\Omega/\square$.

the opposite is true in the Si control. Fig. 20 shows the impact reducing temperature has on f_T for the four base designs. In all three of the SiGe devices, a reduction in temperature leads to an increase in f_T. This is the result of decreases in both τ_b and τ_e. The Si control has an increase in both τ_b and τ_e, which leads to the reduction in f_T as temperature is decreased. A decreasing τ_b causes a reduction in the collector partition noise component and a decreasing τ_e causes a reduction in the emitter shot noise component. Therefore, since τ_b and τ_e have the same temperature dependence, an increase in f_T with reduced temperature is desirable.

VIII. SUMMARY

SiGe HBT's have demonstrated many performance advantages over Si BJT's, including lower broad-band noise. As is summarized in Fig. 21, our simulations suggest that even better noise characteristics can be expected with base designs which are optimized for low-noise performance. In achieving maximum performance, the base thickness is usually limited by technological capabilities while the Ge content is set by thermodynamic stability constraints. As the base thickness is scaled down, the base doping should be scaled up by the same factor to maintain a similar R_{bi}. The Ge profile and doping level can then be tailored to meet the β, R_{bi}, f_T, $f_{\max}$, and $\mathrm{NF}_{\min}$ specifications for the particular application. A minimum emitter width will also have a positive impact on R_{bi} and thus, $f_{\max}$ and $\mathrm{NF}_{\min}$. We demonstrated that the design of the base link resistance is critical because of its strong influence on $f_{\max}$ and $\mathrm{NF}_{\min}$. We introduced a novel Ge profile which allows independent control of β and achieves maximum f_T while maintaining thermodynamic stability. Such a profile can achieve a β of ~200, a peak $f_T > 50$ GHz, a peak $f_{\max} > 60$ GHz, and an $\mathrm{NF}_{\min} < 0.5$ dB at 2 GHz and <1 dB at 10 GHz at 300 K. We also predict that a 45-nm base-width device with a thermodynamically stable flat Ge profile should be able to achieve a $\mathrm{NF}_{\min} < 0.4$ dB at 2 GHz and ~0.8 dB at 10 GHz along with a β of ~300, a peak $f_T > 70$ GHz, and a peak $f_{\max} > 90$ GHz. These 300-K performance values improve as the temperature is reduced. This study suggests that properly designed SiGe HBT's should have broad-band noise performance superior to Si BJT's and competitive with GaAs technologies.

ACKNOWLEDGMENT

The authors would like to thank R. L. Messham, E. Brown, and W. Dubbelday for their valuable support of this work.

REFERENCES

[1] H. Schumacher, U. Erben, and A. Gruhle, "Low-noise performance of SiGe heterojunction bipolar transistors," in *IEEE Microwave Millimeter-Wave Circuit Symp. Dig.*, San Diego, CA, May 1994, pp. 213–216.

[2] D. L. Harame, L. Larson, M. Case, S. Kovacic, S. Voinigescu, T. Tewksbury, D. Nguyen-Ngoc, K. Stein, J. Cressler, S.-J. Jeng, J. Malinowski, R. Groves, E. Eld, D. Sunderland, D. Rensch, M. Gilbert, K. Schonenberg, D. Ahlgren, S. Rosenbaum, J. Glenn, and B. Meyerson, "SiGe HBT technology: Device and application issues," in *IEDM Tech. Dig.*, Washington, DC, Dec. 1995, pp. 731–734.

[3] R. J. Hawkins, "Limitations of Nielsen's and related noise equations applied to microwave bipolar transistors, and a new expression for the frequency and current dependent noise figure," *Solid State Electron.*, vol. 20, pp. 191–196, July 1977.

[4] D. M. Richey, J. D. Cressler, and R. C. Jaeger, "Numerical simulation of SiGe HBT's at cryogenic temperatures," *J. Phys. IV*, Coll. C6 Suppl. in *J. Phys. III*, vol. 4, pp. C6:127–C6:132, 1994.

[5] ——, "Low-temperature modeling of SiGe HBT's using SCORPIO," in *Proc. Electrochemical Soc. Symp. Low-Temperature Electron. High-Temperature Superconductivity*, Pennington, NJ, May 1995, pp. 178–188.

[6] D. M. Richey, J. D. Cressler, and A. J. Joseph, "Scaling issues and Ge profile optimization in advanced UHV/CVD SiGe HBT's," *IEEE Trans. Electron Devices*, vol. 44, pp. 431–440, Mar. 1997.

[7] A. J. Joseph, J. D. Cressler, D. M. Richey, and D. L. Harame, "Impact of profile scaling on high-injection barrier effect in advanced UHV/CVD SiGe HBT's," in *IEDM Tech. Dig.*, San Francisco, CA, Dec. 1996, pp. 253–256.

[8] A. J. Joseph, J. D. Cressler, D. M. Richey, R. C. Jaeger, and D. L. Harame, "Neutral base recombination and its influence on the temperature dependence of Early voltage and current gain–Early voltage product in UHV/CVD SiGe heterojunction bipolar transistors," *IEEE Trans Electron Devices*, vol. 44, pp. 404–413, Mar. 1997.

[9] D. L. Harame, J. M. C. Stork, B. S. Meyerson, K. Y.-J. Hsu, J. Cotte, K. A. Jenkins, J. D. Cressler, P. Restle, E. F. Crabb, S. Sabanna, T. E. Tice, B. W. Scharf, and J. A. Yasaitis, "Optimization of SiGe HBT technology for high-speed analog and mixed-signal applications," in *IEDM Tech. Dig.*, Washington, DC, Dec. 1993, pp. 71–74.

[10] J. W. Matthews and A. E. Blakeslee, "Defects in epitaxial multilayers—Part I: Misfit dislocations in layers," *J. Cryst. Growth*, vol. 27, pp. 118–125, 1974.

[11] ——, "Defects in epitaxial multilayers—Part II: Dislocation pile-ups, threading dislocations, slip lines, and cracks," *J. Cryst. Growth*, vol. 32, pp. 265–273, 1975.

[12] S. R. Stiffler, J. H. Comfort, C. L. Stanis, D. L. Harame, E. de Fresart, and B. S. Meyerson, "The thermal stability of SiGe films deposited by ultrahigh-vacuum chemical vapor deposition," *J. Appl. Phys.*, vol. 70, pp. 1416–1420, 1991.

[13] ——, "Erratum: The thermal stability of SiGe films deposited by ultrahigh-vacuum chemical vapor deposition, *J. Appl. Phys.*, vol. 70, p. 7194, 1991.

[14] E. F. Crabbé, J. D. Cressler, G. L. Patton, J. M. C. Stork, J. H. Comfort, and J. Y.-C. Sun, "Current gain rolloff in graded-base SiGe heterojunction bipolar transistors," *IEEE Electron Device Lett.*, vol. 14, pp. 193–195, Apr. 1993.

[15] D. L. Harame, J. H. Comfort, J. D. Cressler, E. F. Crabbe, J. Y.-C. Sun, B. S. Meyerson, and T. Tice, "Si/SiGe epitaxial-base transistors—Part I: Material, physics, and circuits," *IEEE Trans. Electron Devices*, vol. 42, pp. 455–468, Mar. 1995.

William E. Ansley (S'89) was born in Naples, FL, on September 11, 1965. He received the B.E.E. and M.S. degrees in electrical engineering from Auburn University, Auburn, AL, in 1991 and 1994, respectively, and is currently working toward the Ph.D. degree in electrical engineering.

John D. Cressler (S'86–A'91–SM"91), for photograph and biography, see this issue, p. 589.

David M. Richey (S'88–M'96) received the B.E.E., M.S., and Ph.D. degrees in electrical engineering from Auburn University, Auburn, AL, in 1989, 1991, and 1996, respectively.

In 1996, he joined Lucent Technologies, Allentown, PA, as a Member of Technical Staff. His current research interests include bipolar device modeling, high-performance analog IC design and simulation, and interconnect delay modeling.

Dr. Richey is a member of Eta Kappa Nu, Tau Beta Pi, Phi Kappa Phi, and Sigma Xi.